Contents lists available at ScienceDirect

Acta Materialia

Full length article

Atypical pathways for lamellar and twinning transformations in rapidly solidified TiAl alloy

Xinyu Zhang[a], Chuanwei Li[b,*], Minghui Wu[c,d], Zhenhua Ye[b], Qing Wang[e], Jianfeng Gu[a,b,*]

[a] Shanghai Key Laboratory of Materials Laser Processing and Modification, Shanghai Jiao Tong University, Shanghai 200240, China
[b] Institute of Materials Modification and Modelling, School of Materials Science and Engineering, Shanghai Jiao Tong University, Shanghai 200240, China
[c] College of Materials and Chemical Engineering, MinJiang University, Fuzhou 35108, China
[d] Fujian Key laboratory of Functional marine Sensing materials, Minjiang University, Fuzhou 35108, China
[e] Laboratory for Microstructures, Institute of Materials, Shanghai University, Shanghai 200444, China

A R T I C L E   I N F O

A B S T R A C T

Additively manufactured alloys undergo a rapid solidification process followed by thermal cycles, which promotes the microstructures to return to equilibrium. The microstructural behavior therein is especially complicated and inconceivable at times, thereby greatly restricting the tailorability of microstructures for additive manufacturing. To improve the understanding of microstructure formation in rapidly solidified TiAl alloy, Ti–47Al–2Cr–2Nb powders were aging-treated to reveal the microstructural evolution behavior on multiple scales, and the microstructural transformation mechanisms were comprehensively analyzed from the viewpoints of thermodynamics and kinetics. The results show that the rapidly solidified TiAl alloy almost retains the α_2 phase, which then transforms into nanolamellar structures or equiaxed γ microstructures depending on the temperature. The completely different microstructure selections were determined by the competitive growth of lamellar structures and equiaxed γ grains. More importantly, atypical pathways for lamellar and twinning transformations were first discovered in these microstructural transformation processes. A 6H-type long periodic stacking ordered (LPSO) phase was observed to be in the form of straight laths in the retained α_2 phase, and 9R- and 18R-type LPSO phases were discovered in the equiaxed γ grains. The 6H-type LPSO phase transformed into nano γ laths, whose formation driving force was deduced to result from the extremely high elastic energy stored in the retained α_2 phase. The 9R- and 18R-type LPSO phases transformed into a more stable γ_{twin} phase to reduce the entire energy of the system. This research may potentially enhance the understanding of the microstructure of additively manufactured TiAl alloy and consequently, the tunability of such microstructure as required.

© 2022 Acta Materialia Inc. Published by Elsevier Ltd. All rights reserved.

1. Introduction

Additive manufacturing (AM) is a great innovation in manufacturing technology because it subverts the conventional idea—fabricating a part by removing it from an ingot; complex components can be directly fabricated by multilayer accumulation [1]. Concomitantly, owing to the rapid solidification and multiple thermal cycles during the manufacturing process, the AMed alloys usually exhibit certain notable microstructural features, some of which are extraordinary and can potentially lead to breakthroughs in mechanical properties [2–4]. Intermetallic TiAl alloys, which are among the most promising high-temperature structural materials, are attracting much interest in aerospace applications. Additionally, research on AMed TiAlalloys began in the last decade, and the re-

lated microstructural characterizations have been conducted intensively ever since [5–7]. It is revealed that the phase constitutions and microstructural morphologies vary greatly depending on the processing parameters, and almost all the microstructures having been observed in the alloys, such as lamellar, duplex, and near gamma structures, can be directly obtained by carefully tailoring the manufacturing process [7–9]. In our recent studies, Ti–47Al–2Cr–2Nb alloys containing special alternately layered microstructures were fabricated by direct laser deposition, and some long periodic stacking ordered (LPSO) phases, formed therein, contributed to the excellent mechanical properties of the alloys [10,11].

LPSO phase has a complicated long-range structure, and both rhombohedral (R) and hexagonal (H) Bravais lattices can form depending on the stacking period of the closed-packed atomic layers. The present studies on the LPSO phase mainly concentrate on rare-earth-containing Mg alloys, and their microstructures, crystallography, transformation processes, and strengthening mechanisms have been widely reported. For instance, Abe et al. [12] identified

* Corresponding author.
  E-mail addresses: li-chuanwei@sjtu.edu.cn (C. Li), gujf@sjtu.edu.cn (J. Gu).

the formation of a novel LPSO phase with a 6H structure (ABCBCB) in a warm extruded $Mg_{97}Zn_1Y_2$ alloy, whose unit cell comprised six close-packed planes of the Mg crystal accompanied by Zn and Y elements in certain planes. In addition, many other types of LPSO phases form in these alloys. On the basis of thermodynamic calculation and experimental observation, Kim et al. [13] proposed a transformation sequence of the precipitated LPSO phase in α-Mg matrix: a single building block generated by a Shockley partial dislocation sliding on a specific lattice plane → various metastable LPSO building block clusters → 14H, providing that 14H is the most stable structure among these LPSO phase types. Moreover, Matsuda et al. [14,15] revealed that the LPSO phase not only suppresses the formation of deformation twins and basal-plane dislocations, but also activates the dislocations on non-basal planes, thereby enhancing the mechanical properties of Mg alloys.

The presence of LPSO phases in TiAl alloys has been reported since the 1990s; Singh and Appel et al. [16,17] initially identified a three-plane deformation-induced structure (9R) adjacent to pre-existing twins in a highly deformed Ti–48.5Al–1.5Mn alloy. Then, Wang et al. [18] identified the stacking sequence of the 9R structure to be …ABCBCACABA… by high-resolution transmission electron microscopy (HR-TEM) and suggested that its formation mechanism can be attributed to the periodically arranged Shockley partial dislocations around incoherent twin or incoherent pseudo twin boundaries. There has been no further investigation until recently. Song et al. [19] discovered another type of 6H structure at the nanoindentation zone in a high-Nb-containing TiAl alloy from the selected area electron diffraction (SAED) pattern, but the characterization was not much detailed. In addition, there have been controversies regarding the LPSO phase in TiAl alloys. Chen et al. [20] claimed that the overlapping of α_2/γ laths or γ/γ_{twin} laths could result in a double diffraction, which might mislead our identification of the LPSO phases. To date, there are limited studies on the LPSO phase in γ-based TiAl alloys. The crystallography, formation mechanism, and effects of these LPSO phases need to be further investigated.

Although we have observed LPSO phases in AMed Ti–47Al–2Cr–2Nb alloy and characterized their stacking sequences on an atomic scale, there are some questions on the manner of formation of these structures and if they are intermediate structures during their transformation from a rapidly solidified state to equilibrium. Meanwhile, because only a few previous studies have focused on this transformation behavior and the investigations are limited to individual conditions and scales [21–23], there is insufficient information to fully understand the microstructural evolution process and the formation mechanism of LPSO phase in nonequilibrium TiAl alloys. Thus, it is imperative to conduct a complete, systematic investigation to address these gaps.

In this work, a series of aging treatments on rapidly solidified TiAl powders were conducted to investigate the transformation behaviors at various temperatures. The multiscale microstructural characterizations and the intermediate structures during the return to the equilibrium were emphasized. Moreover, the corresponding microstructure selections and formation mechanisms were analyzed from the aspects of thermodynamics and kinetics. The results could provide a new perspective on understanding the phase transformation mechanism occurred in AMed TiAl alloys.

2. Material and experimental

The rapidly solidified (RS) materials are Ti–47Al–2Cr–2Nb (at.%) powders with the diameters ranging from 53 to 105 μm. Our preliminary aging treatments reveal that the RS microstructure would transform into lamellar and equiaxed microstructure when the RS powders were aging-treated at 700 and 900°C for 30 min, respectively. Then, two series of aging treatments with various aging time at these two temperatures were conducted to investigate a more detailed microstructural evolution process. Prior to these aging treatments, the powders were sealed in vacuum quartz tubes to protect them from oxidation. The quartz tubes were placed in a furnace that was heated to a target temperature; immediately after the aging time, the tubes were directly quenched to room temperature in water.

The phase constitution of the as-rapidly-solidified and aging-treated powders was identified by a multifunctional X-Ray diffraction (XRD) instrument (D8 ADVANCE Da Vinci, Bruker, Germany) with a Cu-Kα radiation at 40 kV and 40 mA, and the diffraction angle (2θ) was varied from 30° to 90° with steps of 0.02° and a scanning rate of 2° min^{-1}. The microstructural morphology was characterized from the backscattered electron (BSE) images and electron backscatter diffraction (EBSD) images obtained by field emission scanning electron microscopy (SEM) (LYRA3 GMU, TESCAN, Czech Republic) at 20 kV. The EBSD analysis of whole particles and locally magnified regions were conducted with the steps of 0.15 μm and 0.04 μm, respectively. The chemical composition was measured by the energy dispersive X-ray spectroscopy (EDS) equipped on SEM, and linear scanning was used to determine the chemical distribution in the selected regions. The powders for BSE, EDS, and EBSD characterizations were embedded in conductive resins which were then grounded and polished following a standard process. Additional information on the detailed microstructures was revealed by transmission electron microscopy (TEM), which was performed on a field emission microscope (TALOS F200X, FEI, USA) at 200 kV. Thin slices used for TEM observation were cut from the areas of interest in the powders using focused ion beam technology. Ion cleaning was carried out for several minutes to remove the impurities on the surfaces prior to the HR-TEM observations.

The calculations of formation energy were based on density functional theory (DFT) using the projector-augmented wave (PAW) method implemented in the Vienna ab-initio simulation package [24]. The Perdew–Burke–Ernzerhof functional [25] was adopted to model the electron exchange-correlation. The energy cutoff of the plane waves was set to 300 eV. The Monkhorst–Pack method was used to sample the Brillouin zone, and the K-points mesh was set to $2 \times 2 \times 2$ for the supercell and $7 \times 7 \times 7$ for the primitive cell [26]. The convergence tolerance for the force during structure relaxation was set to 0.01 eV Å^{-1} for every atom.

3. Results

3.1. Microstructures of rapidly solidified TiAl powders

First, the initial microstructure of the RS TiAl powder was characterized. The BSE image reveals a dendritic morphology, wherein the dendrites exhibit grey contrast with a white narrow skeleton in the dendrite core, while the interdendrites exhibit dark contrast (Fig. 1a). Because a BSE image mainly reflects the atomic number contrast, Fig. 1a signifies the chemical fluctuations in these powders. Linear chemical distribution analysis indicates that the dendrite is rich in Ti and Nb while the interdendrite is rich in Al and Cr (Fig. 1b). This dendritic segregation phenomenon is usually related to the solidification behaviors in which Al and Cr are repelled to the interdendrites when the dendrites first solidify from the liquid [27]. Additionally, although the XRD profile appears to be in accordance with the α_2 phase (Fig. 1c), it is difficult to distinguish the ordered α_2 phase from the disordered α phase because the phases have overlapped diffraction profiles in this diffraction range, and some studies reported that the disordered α phase can be the predominant phase in RS TiAl powders [21]. Thus, the electron diffraction was conducted to assist in the identification of the primary phase. Superlattice diffraction spots are clearly observed when the incident beam is along the $[11\bar{2}0]_{\alpha_2}$ axis (Fig. 2a),
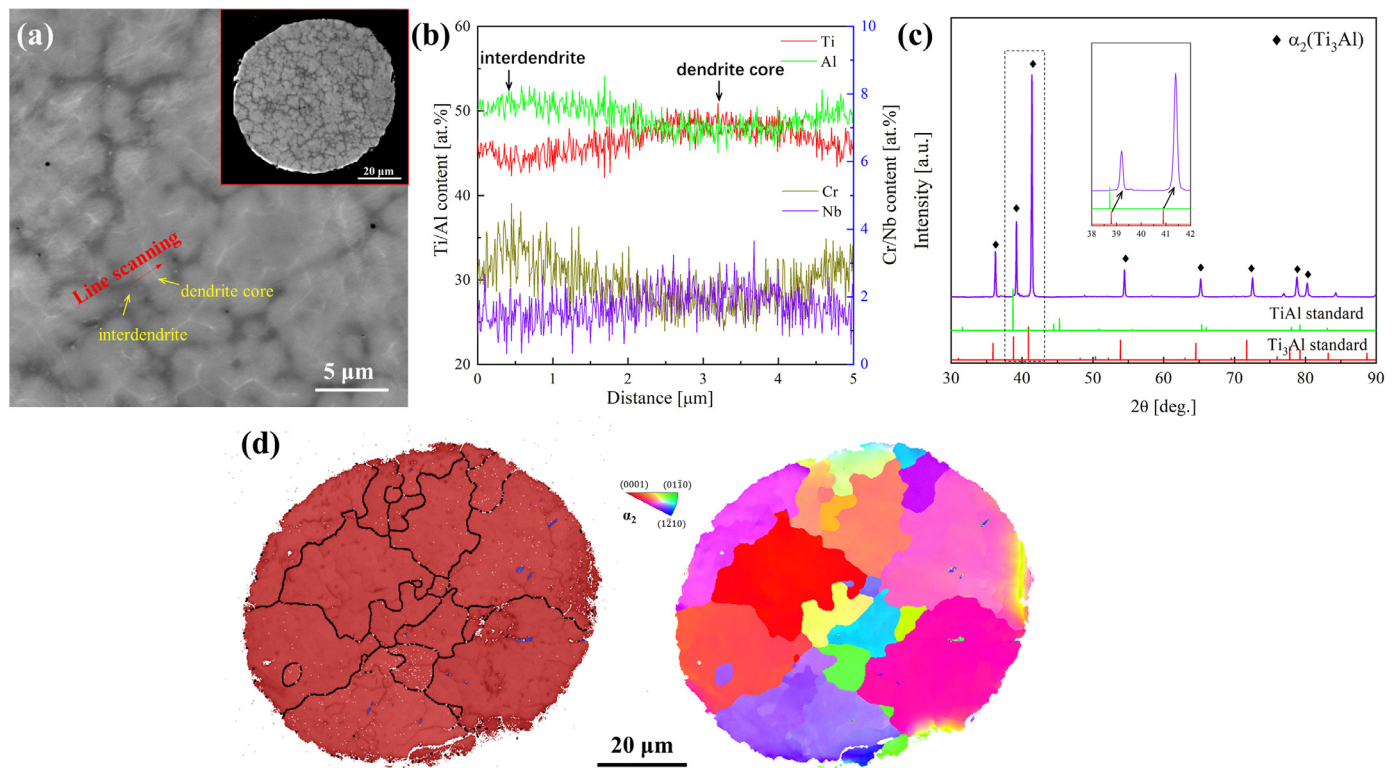
Fig. 1. (a) BSE image of the RS Ti–47Al–2Cr–2Nb alloy, showing a dendritic microstructural morphology. (b) Chemical distribution across both dendrites and interdendrites corresponding to the line scanning denoted in (a). (c) XRD pattern of the RS powder compared with the standard diffraction patterns of α_2(Ti$_3$Al) and γ(TiAl) phases. The lattice information (for α_2 phase, a = 5.7640 Å, c = 4.6640 Å; for γ phase, a =3.9139 Å, c = 3.9968 Å) is obtained by the first-principles approach with full relaxation, and the diffraction information is obtained using CrystalMaker software. The inserted diffraction pattern is a locally magnified image comparing the peak shift with the standard α_2 diffraction pattern. (d) The phase maps (the red and blue respectively represent α_2 and γ phases) and inverse pole figure (IPF) images of the RS powders.
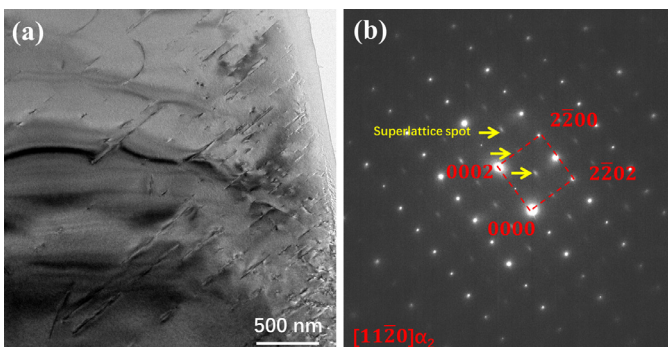

Fig. 2. (a) Bright field (BF) image of the RS powders and (b) its corresponding $[11\bar{2}0]_{\alpha2}$ SAED pattern, wherein the yellow arrows denote the superlattice spots in the SAED pattern.

which demonstrates that the microstructure mainly consists of an ordered α_2 phase. Quantitative phase analysis based on the XRD results reveals that the α_2 and γ phases constitute 93.10 wt.% and 6.90 wt.%, respectively. This is in accordance with the EBSD analysis—large α_2 grains occupy the majority of the powders and only a few small γ grains are distributed in the α_2 grains (Fig. 1c). However, this phase constitution largely deviates from the equilibrium state wherein γ phase occupies the majority (approximately 81.43 wt.% for Ti-47Al, as calculated by Thermocalc software). This nonequilibrium microstructure is attributed to the rapid cooling rate (10^4–10^6 K·s^{-1}) during the atomization process, thus, most of the high-temperature α phase can transform into the retained α_2 phase via just an ordering reaction [22,28]. Additionally, the lattice parameters of the retained α_2 phase are low because their diffraction peak is slightly shifted to the right (Fig. 1c).

3.2. Lamellar structure and the 6H-type LPSO phase

When the RS powders were aging-treated at 700°C, the microstructure would transform into lamellar structure; the associated microstructure characterizations are presented as follows. As is known, the RS microstructure is almost composed of retained α_2 phase and no diffraction peak of γ phase can be observed in the XRD pattern (Fig. 1c). When these powders are aging-treated for 5 min, the diffraction peaks, corresponding to $(20\bar{2}0)_{\alpha2}$, $(0002)_{\alpha2}$ and $(20\bar{2}1)_{\alpha2}$, at 35.8°, 38.7°, and 40.8°, respectively, are still the main features in the XRD pattern (Fig. 3a). However, forked peaks are notably observed at 38.5°, and a very weak peak is located at 45.1° (Fig. 3b). The left forked peak and weak peaks correspond to the $(111)_{\gamma}$ and the unresolved $(002)_{\gamma}/(200)_{\gamma}$, respectively, signifying that the retained α_2 phase starts transforming into the γ phase. As the aging time increases, the intensities of the three major α_2 diffraction peaks gradually decrease, and the intensities of the γ diffraction peaks increase significantly. When the aging time reaches 4 h, the α_2 diffraction peaks disappear, and all the diffraction peaks correspond to the γ phase, indicating that the retained α_2 phase almost completely transforms into the γ phase. The $\alpha_2\rightarrow\gamma$ phase transformation process is also revealed by the phase distribution maps based on EBSD analysis (Fig. 4), and the content of the γ phase increases from 37.4 wt.% to 91.9 wt.% as the aging time increases from 5 min to 4 h.

Fig. 4(a3-d3) presents the magnified BSE images of these powders, wherein the primary boundaries of the initial α_2 grains can be distinguished and very fine lamellar structures fill in the primary α_2 grains (because these lamellae are extremely thin, some of them may not be clear in these figures, but these lamellar structures are identifiable by TEM, as shown in Fig. 5). Moreover,
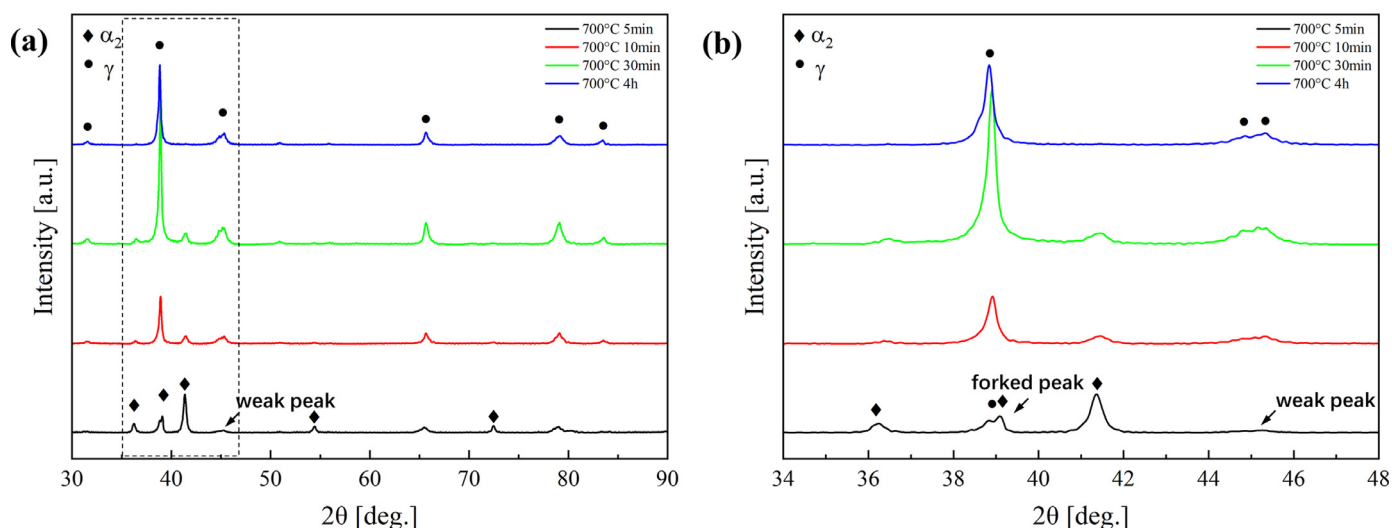
Fig. 3. (a) General XRD patterns of the powders aging-treated at 700°C for different times and (b) magnified patterns of the dotted rectangle in (a) with 2θ ranging from 34° to 48°.

the lamellar orientations in the adjacent α_2 grains are different, as indicated by the red dotted lines. Besides, it is observed that some granular γ grains have precipitated at the primary boundaries when the aging time reaches 30 min, and more granular γ grains forms at the primary boundaries when the time increases to 4 h (Fig. 3d).

Fig. 5 presents the TEM images of the lamellar structures with respect to increasing aging time. When the powders are aging-treated for 5 min, some lamellae have been seen in the primary α_2 grains (Fig. 5a). In the inserted SAED pattern for $<11\bar{2}0>_{\alpha 2}$ zone axis, the ordered α_2 diffraction pattern is clearly distinguished. Moreover, there is a series of closely arranged diffraction spots found along the $[0002]_{\alpha 2}$ axis, locating at $1/6(0002)_{\alpha 2}$, $2/6(0002)_{\alpha 2}$, $3/6(0002)_{\alpha 2}$, $4/6(0002)_{\alpha 2}$, and $5/6(0002)_{\alpha 2}$, and so on, respectively. The corresponding HR-TEM image shows that periodic stripes with atom plane configuration occur in the precipitated lamellae; these lamellae result in the closely arranged diffraction spots (Fig. 5b). This diffraction pattern appears different from that of the common α_2/γ lamellar structures in TiAl alloys. Previously, Chen et al. [20] attributed the occurrence of six times reflection to the double diffraction caused by the overlapping of α_2 and γ lamellae. However, in our experiment, the specimen was tilted to ensure that the incident beam exactly along the $<11\bar{2}0>_{\alpha 2}$ axis and the lamellar interfaces were completely edge-on; thus, the α_2 and γ phases could not overlap. Even in the case of a slight deviation, the overlapping region should not be so wide (approximately 11.5 nm). Therefore, it is deduced that the precipitated lamellae belong to a certain LPSO phase. Moreover, the R and H structures can be identified from the diffraction patterns under the [010] zone axis; the diffraction pattern indicates H structure if the angle between the (00l) and (10l) diffraction spots is 90°, else it indicates R structure [29]. Fig. 6 presents the atomic stacking images of the precipitated LPSO lamella and its corresponding fast Fourier transformation (FFT) image. Although there is some random atomic arrangement, …ABCBACA… is the dominant stacking sequence; the atoms in the first and seventh layers are at position A, and each of the six layers cyclic (Fig. 6b). The angle between (006) and (100) is measured as 90° (Fig. 6c). All these demonstrate that this structure denotes a hexagonal structure with six stacking layers, i.e., 6H. Meanwhile, the α_2 phase with …ABA… stacking sequence is also presented in Fig. 6d. The orientation relationship between the 6H phase and α_2 matrix is deduced as $(006)_{6H} \parallel (0001)_{\alpha 2}$, $[010]_{6H} \parallel [11\bar{2}0]_{\alpha 2}$.

When the aging time is increased to 30 min, almost all the α_2 grains transform into very fine lamellar structures so that the α_2 diffraction spots can be hardly found in the SAED image. The lamellar structures are mainly composed of the twinned γ lamellae. The thickness of these lamellae notably reduces to about 1 nm (Fig. 5d). Meanwhile, the 6H structures are no longer observed. When the aging time is increased to 4 h, the lamellar structures are still composed of the twinned γ lamellae, but their thickness has increased to 5–15 nm (Figs.5e and f). In addition, some ledges also appear at the lamellar interfaces. Throughout the lamellar formation process, 6H structures are temporarily observed at the initial stage of the transformation, then they disappear, leaving only the twinned γ lamellae; this implies that the 6H structure is probably an intermediate structure in the lamellar transformation process. Its detailed transformation mechanism will be discussed in 4.2 Section.

3.3. Equiaxed γ microstructure and the 9R-and 18R-type LPSO phase

The microstructures, with respect to increasing aging time at 900°C, were characterized to explore the microstructural evolution. The XRD results show that even if the powders were aging-treated at 900°C for only 5 min, the retained α_2 phase almost completely transforms into the γ phase (Fig. 7a). Moreover, some forked peaks such as $(002)_\gamma/(200)_\gamma$, $(202)_\gamma/(220)_\gamma$, and $(113)_\gamma/(311)_\gamma$ can be observed in the diffraction pattern. These forked peaks are related to the tetragonal crystal of the γ phase, whose a is not equal to c.

However, as the time increases, a weak $(20\bar{2}1)_{\alpha 2}$ diffraction peak occurs at 40.8° and its intensity slightly increases, which implies that an inverse $\gamma \rightarrow \alpha_2$ transformation occurs during the aging process. The occurrence of the inverse $\gamma \rightarrow \alpha_2$ transformation from the nonequilibrium to equilibrium is an unusual phenomenon; Guyon et al. [21] also discovered this behavior in the Ti–48Al–2Cr–2Nb powders that underwent a continuous heating process. Meanwhile, the forked features are more obvious, some of which even separated into two individual peaks, indicating that the c/a value increases gradually. The EBSD analysis reveals that the primary α_2 grains completely transform into small equiaxed γ grains ($\sim 1~\mu$m); their microstructural morphology and grain size show no obvious changes as the aging time increases (Fig. 8(a1-d1)). In addition, there are certain paralleled or interlaced laths occurred in the equiaxed γ grains, as indicated by the yellow arrows in Fig. 8(a2-d2).
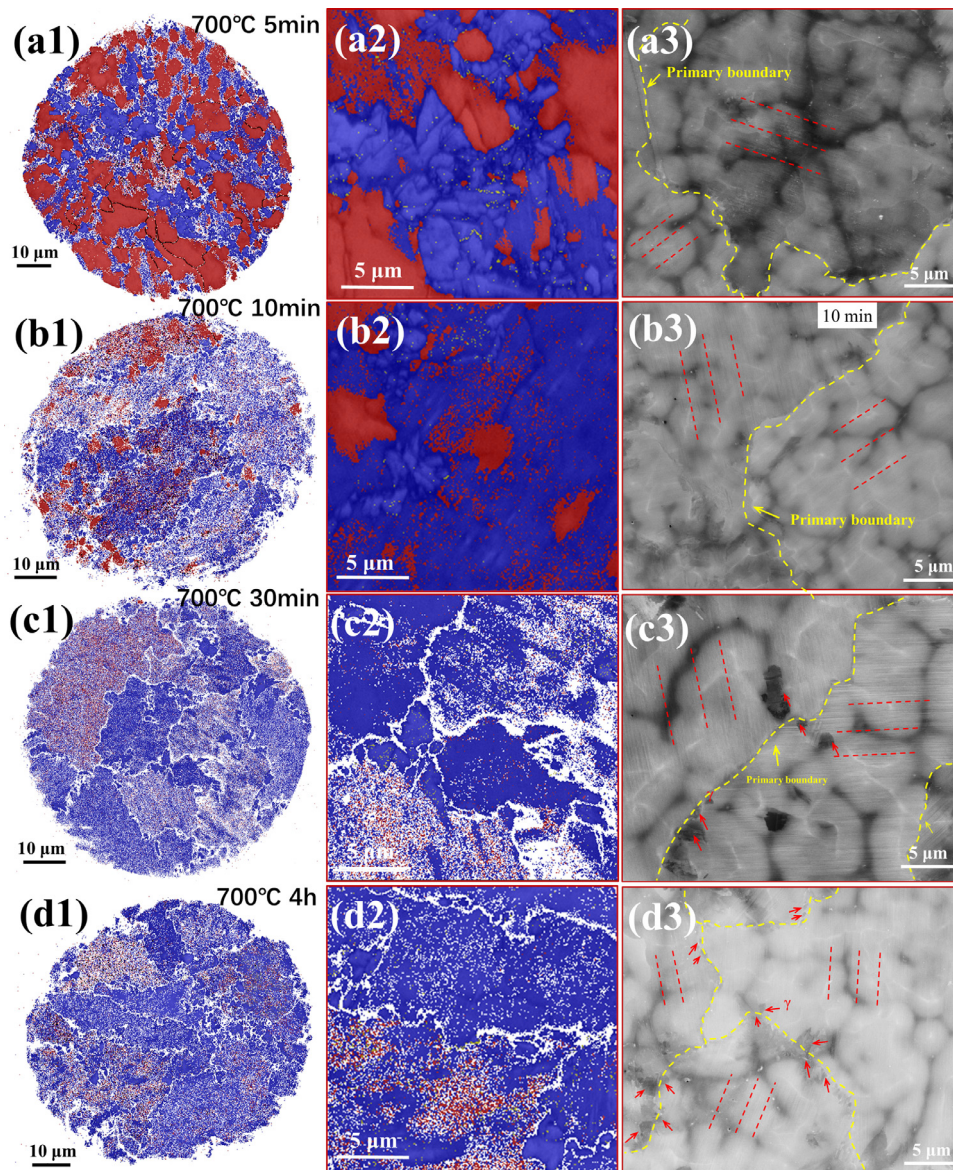
Fig. 4. Microstructural morphology of the powders aging-treated at 700°C. (a1-d1) Phase maps of whole powders as the holding time increases from 5 min to 4 h. The α_2 and γ phases are represented in red and blue, respectively; (a2-d2) Phase maps of locally magnified regions in (a1-d1); (a3-d3) Corresponding BSE images of the powders. The yellow dotted lines, red dotted lines, and red arrows denote the boundaries of primary α_2 grains, lamellar orientations in the primary α_2 grains, and γ grains distributed around the primary boundaries.

Although there seems no obvious change in the appearance of equiaxed γ grains with increasing aging time, their interior structure gets evolved. The TEM images reveal many straight laths inside the equiaxed γ grains (Fig. 9), and mirrored diffraction spots are distinguishable in the SAED patterns, indicating the existence of γ twins. The corresponding dark field (DF) image and the HR-TEM image show that the γ twins exist in the form of straight laths (Fig. 9(a1)) and the twinning plane is $(111)_\gamma$. In addition to these γ_{twin} laths, some unusual structures with periodic stripes are observed in the γ matrix when the aging time is 5 min or 30 min (Figs.9(a3),(a4),(b2)), whose diffraction patterns exhibit three or six times spots, respectively, along the $<111>_\gamma$ axis, as inferred from the inserted FFT images. Because these HR-TEM images were obtained along $<1\bar{1}0>$ or $<101>$ axes and the twinning planes were edge-on, these periodic stripes are not the false images caused by the overlapping of γ and γ_{twin}; the special structures indeed existed. These structures are characterized in the magnified im-

ages (Fig. 10 and Fig. 11); their stacking sequence is determined to be either ...ABCBCACABA... or ...ABCABCBCABCACABCABA... with a stacking period of 6 or 18 layers, respectively. Moreover, because their diffraction spots exhibit a three- or six-fold close-packed feature along the $[111]_\gamma$ axis, and the angles of the two diffraction spots close to the transmission spot are measured as 84.67° and 87.44°, it is deduced that these structures belong to the LPSO phases with 9R and 18R structures, respectively [11,30]. Additionally, their orientation relationships with the γ matrix can be determined as: $(006)_{9R} \parallel (111)_\gamma$, $[010]_{9R} \parallel [1\bar{1}0]_\gamma$ or $(00.18)_{18R} \parallel (111)_\gamma$, $[010]_{18R}$. Aside from the relationship, long laths containing complex features are observed in the γ matrix. Both the 9R and γ_{twin} structures are distinguishable in a single lath, and their transition regions are observed directly (Fig. 12). However, when the aging time is increased to 4 h, the LPSO structures disappear and only the thickened γ_{twin} laths and abundant dislocations remain in the γ grains (Fig. 9(c1,c2)).
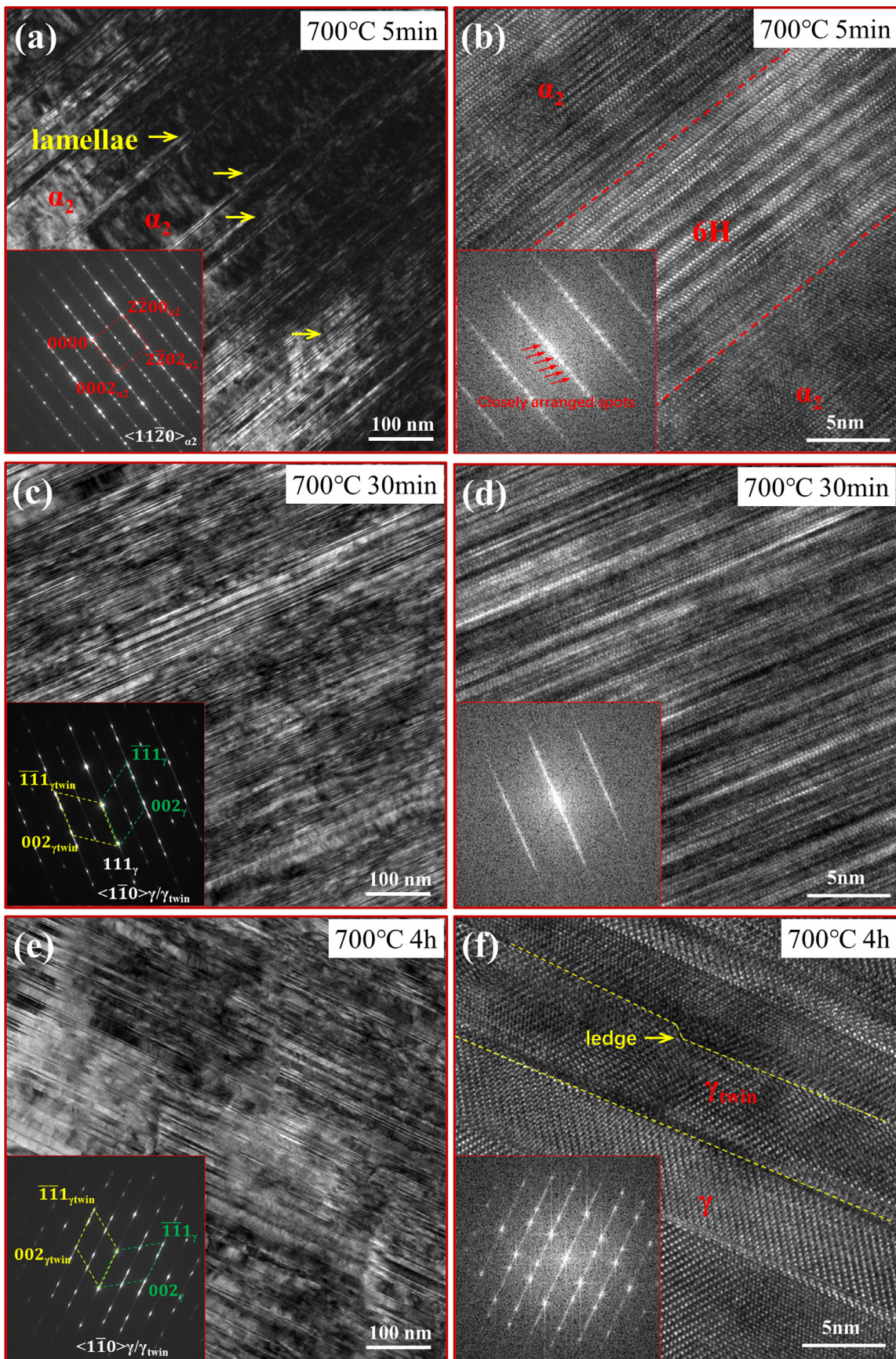
Fig. 5. BF and HR-TEM images of the lamellar structures in the powders aging treated at 700℃. (a, b) 5 min; (c, d) 30 min; (e, f) 4 h. The SAED patterns and FFT images were inserted in the BF and HR-TEM images, respectively.
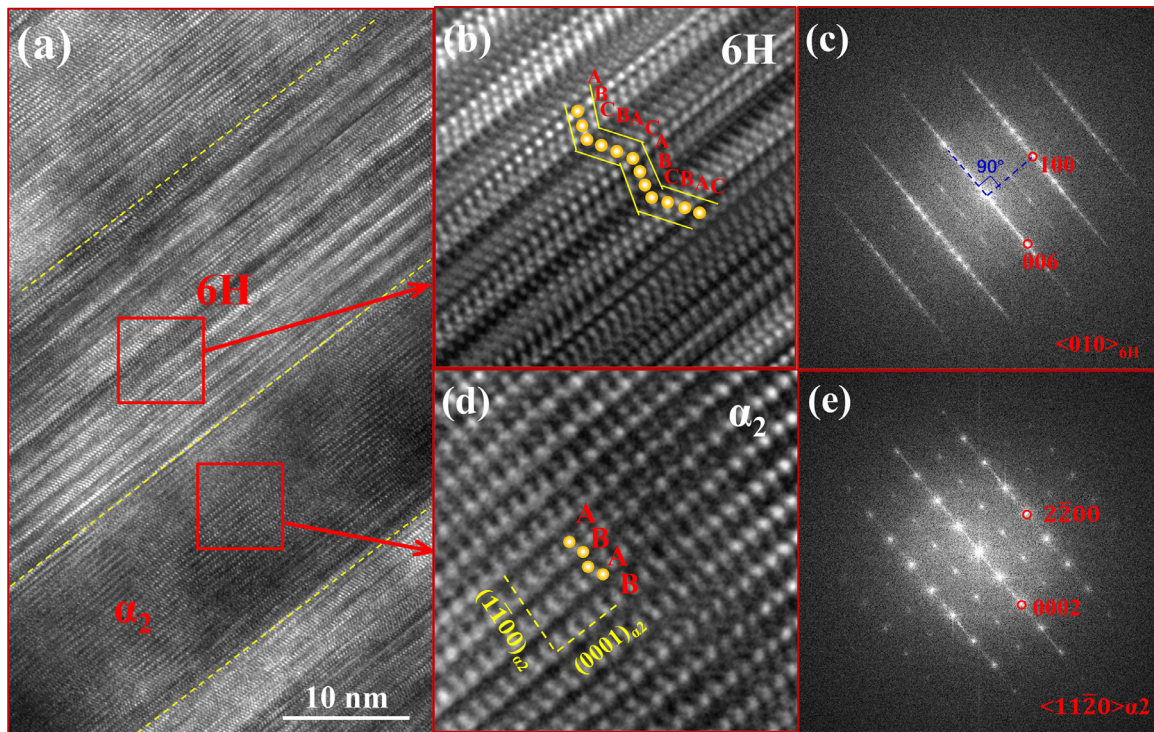
Fig. 6. (a) HR-TEM image of the 6H/α_2 laths. (b, c) Magnified HR-TEM image of the 6H laths and its corresponding FFT image; (d, e) Magnified HR-TEM image of the α_2 matrix and its corresponding FFT image.
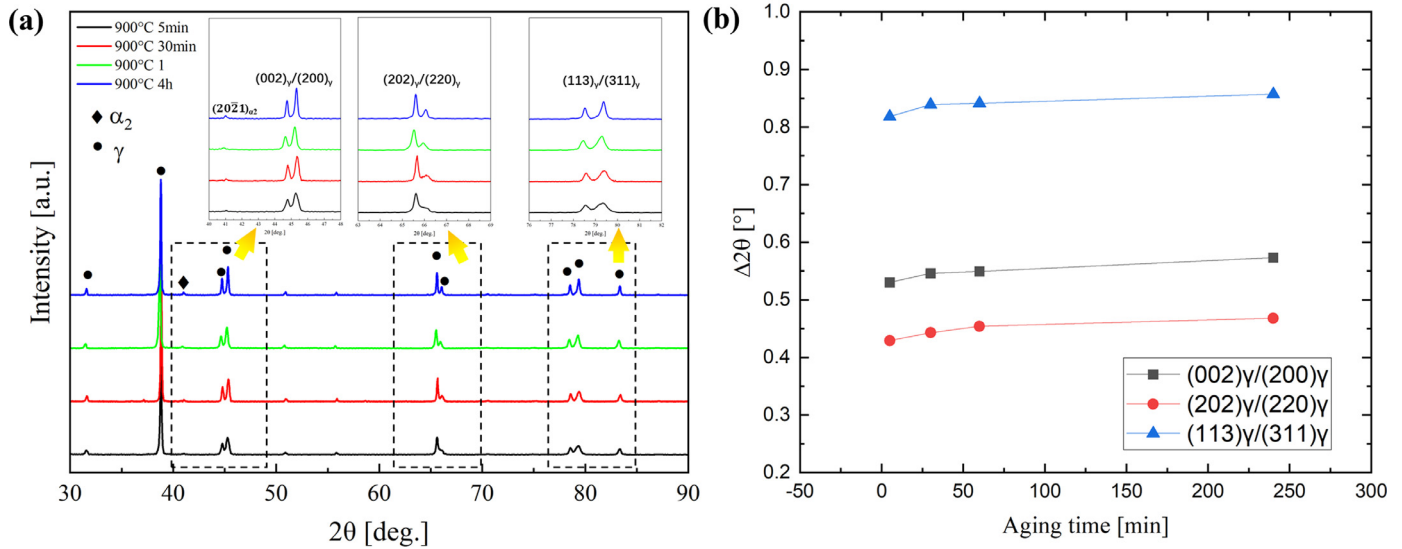

Fig. 7. (a) XRD patterns of the powers aging-treated at 900℃ for different times and the magnified profiles corresponding to $(002)_\gamma/(200)_\gamma$, $(202)_\gamma/(220)_\gamma$, and $(113)_\gamma/(311)_\gamma$ peaks. (b) Splitting degrees as a function of the aging time.

4. Discussion

The above observations demonstrate that RS Ti–47Al–2Cr–2Nb alloy powders can transform into different microstructural morphologies depending on the aging temperature. Moreover, some unusual structures, seldom observed in TiAl alloys before, appear at the preliminary formation stage in the lamellar structure and in the equiaxed γ microstructures. They seem similar to those observed in AMed TiAl alloys, as reported in our previous work [10,11]. The following sections will focus on the microstructural evolution mechanisms based on thermodynamics and kinetics; 4.1 Section discusses the microstructural morphology evolution from a

macroscopic perspective and 4.2 and 4.3 Section discuss the atypical lamellar and twinning transformation observed in our experiments.

4.1. Selection of the lamellar structure and equiaxed γ structure

According to the Ti-Al binary phase diagram [31], the Ti–47Al alloy undergoes a continuous phase transformation process ($L{\rightarrow}L{+}\beta{\rightarrow}\alpha{\rightarrow}\alpha{+}\gamma{\rightarrow}\alpha_2{+}\gamma$) when it solidifies to room temperature in an equilibrium, and the γ phase will occupy a majority in the final microstructure. However, for the rapidly solidified Ti–47Al–2Cr–2Nb powders in the present studies, the room-
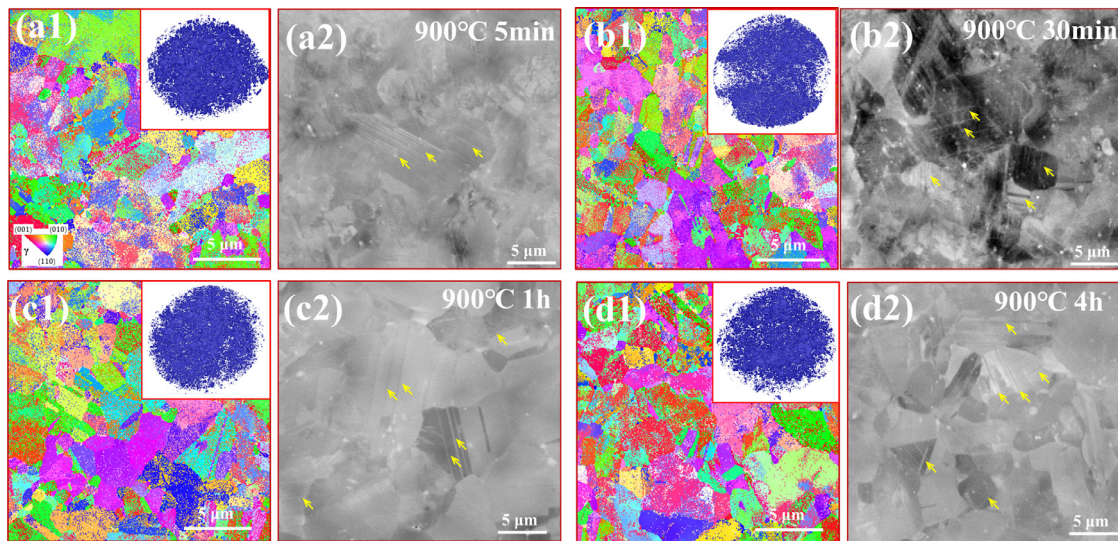
Fig. 8. Microstructural morphology of the powders aging treated at 900°C as the aging time increases from 5 min to 4 h. (a1-d1) IPF images; phase maps of the whole powder are inserted at the right top corner; in the phase maps, the α_2 and γ phases are represented in red and blue, respectively. (a2-d2) Magnified BSE images, wherein the yellow arrows denote the nanolaths in equiaxed γ grains.
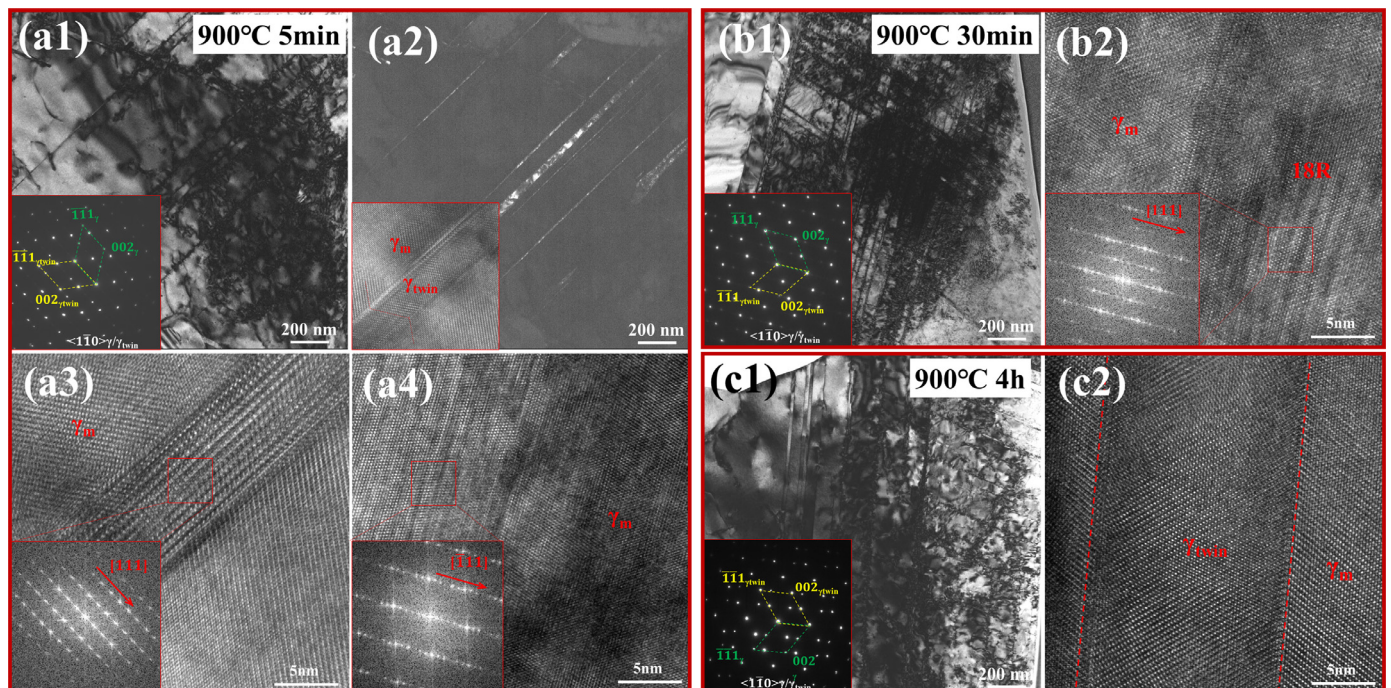

Fig. 9. TEM images of the the powders aging-treated at 900°C. (a1–a4) 5 min; (b1, b2) 30 min; (c1, c2) 4 h. (a1, b1, c1) BF images of the equiaxed γ grains with SAED images inserted; (a2) DF image of the γ_{twin} laths corresponding to the $(002)_{\gamma twin}$ spot in (a); (a3, a4, b2) HR-TEM images of the special structures in the γ matrix with the FFT images inserted; (c2) HR-TEM image of the γ_{twin} lath with straight boundaries.

temperature microstructure is almost completely α_2 phase; it will return to the equilibrium during the subsequent aging treatments. Two microstructural features including nanolamellar and equiaxed microstructures can be obtained by aging-treated at 700 and 900°C, respectively. Similar microstructures have been observed in Guyon's study [21], which focused on a continuous heating process. To explore the microstructure formation mechanism and the competition between the lamellar structure and equiaxed grains, their nucleation and growth processes were analyzed.

4.1.1. Lamellar structure

Usually, in α_2 phase, the occurrence of $1/3<10\bar{1}0>_{\alpha 2}$ partial dislocations on the close-packed plane generate stacking faults

and local fcc structures in the α_2 phase, which serve as the primary nuclei for the lamellar structures [32]. As the accumulation of Al lowers the stacking fault energies in the α_2 phase [33,34], the lamellar structures preferably originate at the interdendrites. However, the transformation process of the lamellar structures has been debated for a long time, and a plausible displacive-diffusive mechanism was finally proposed, which states that the transformation exhibits martensitic crystallography but requires a short-range diffusive flux through the interfacial disconnections [35]. Moreover, Qin et al. [35] focused on lamellar formation and established a growth kinetics model based on a ledge-controlled mechanism (Fig. 13), which agrees well with the experimental observations. In our experiments, ledges were frequently observed at the lamellar
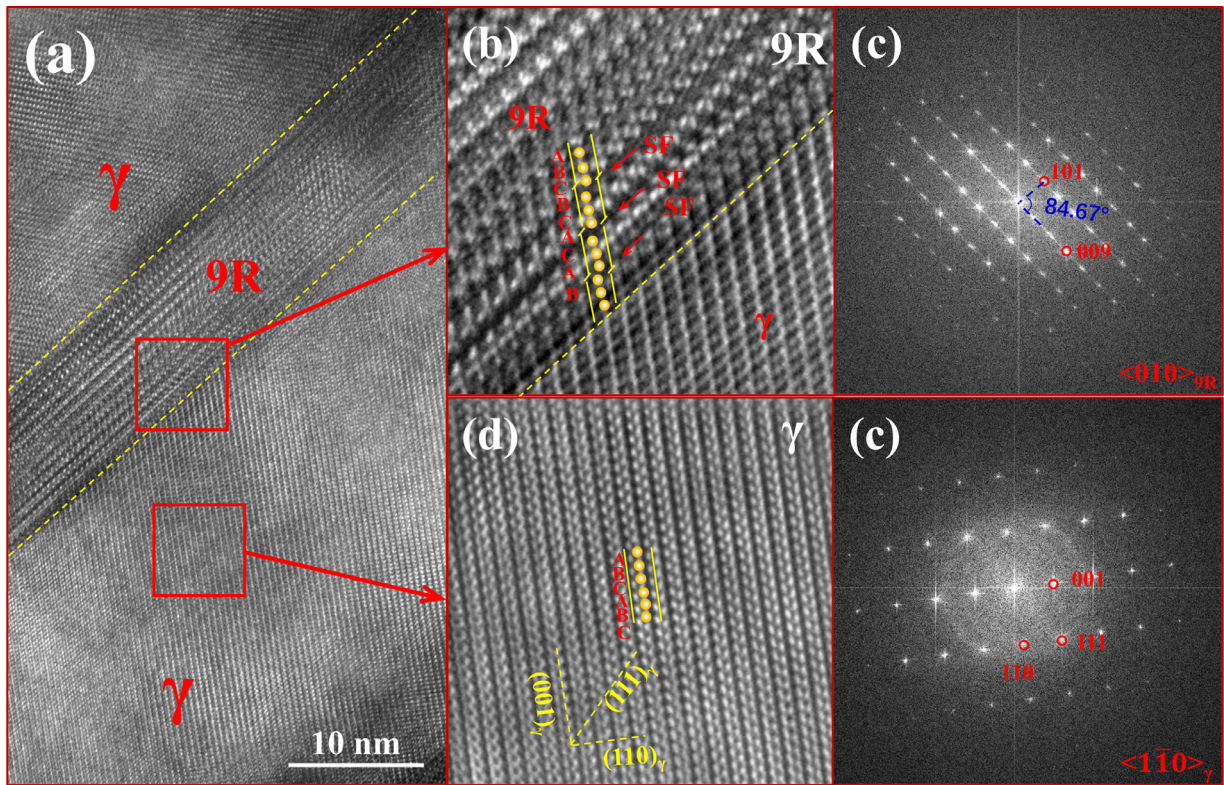
Fig. 10. HR-TEM image of the 9R structure in the equiaxed γ grain. (b, c) Magnified HR-TEM image of the 9R structure and its corresponding FFT image. (d, e) Magnified HR-TEM image of the γ matrix and its corresponding FFT image.
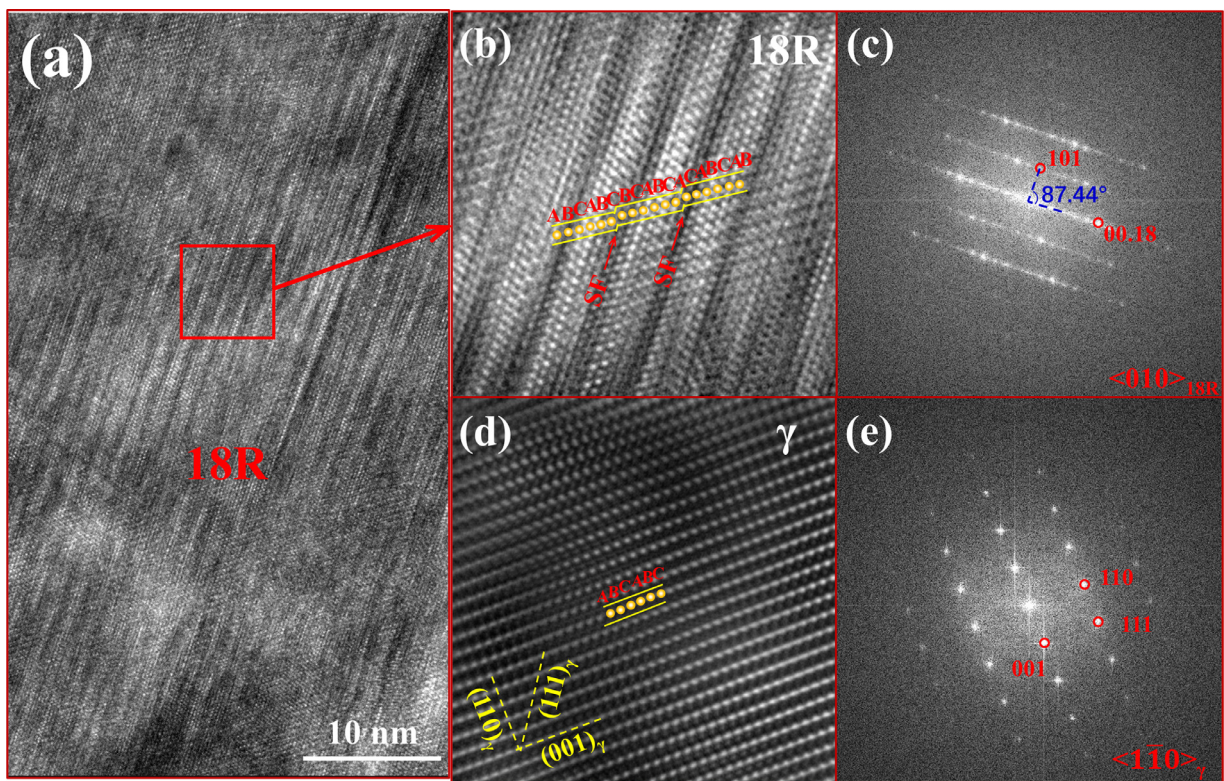

Fig. 11. HR-TEM image of the 18R structure in the equiaxed γ grain. (b, c) Magnified HR-TEM image of the 18R structure and its corresponding FFT image. (d, e) Magnified HR-TEM image of the γ matrix and its corresponding FFT image.
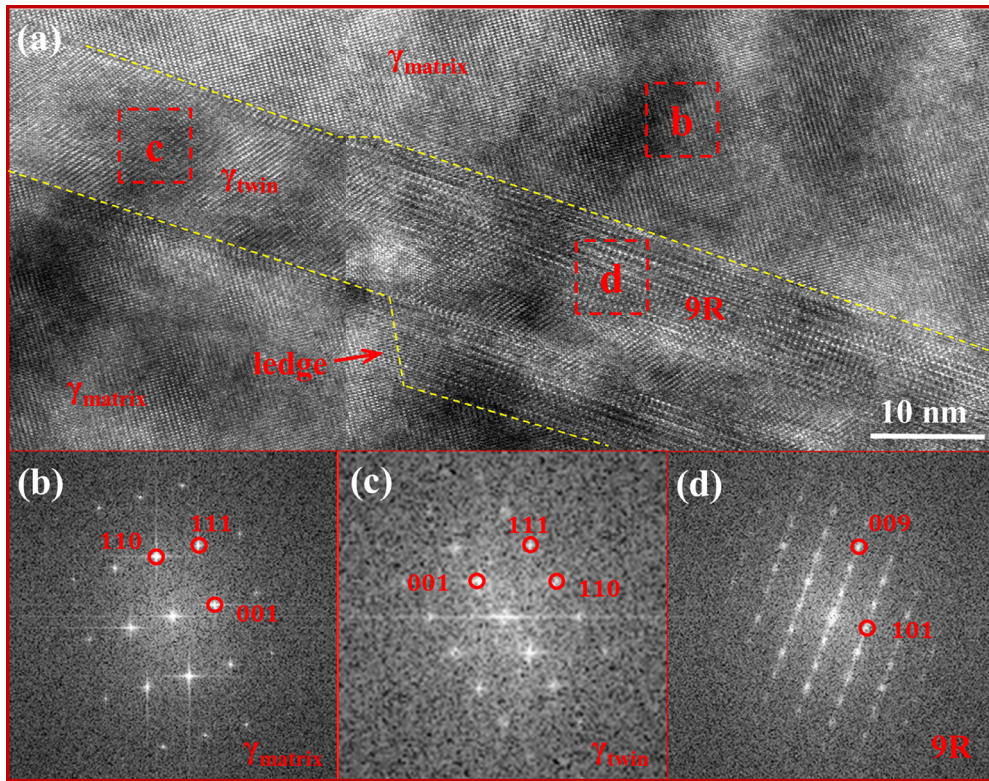
Fig. 12. (a) Transition region between the 9R structure and γ_{twin} lath. (b–c) FFT images of the γ matrix, γ_{twin} lath, and 9R structure corresponding to the rectangles denoted in (a), respectively.
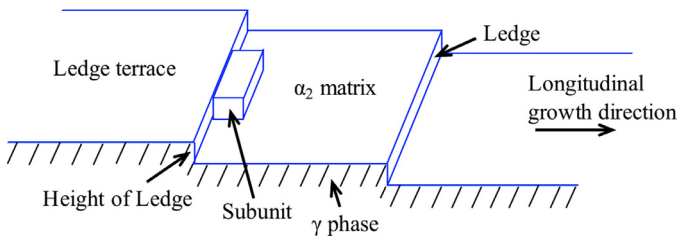

Fig. 13. Schematic of the ledge mechanism of γ lath in the retained α_2 phase.

Fig. 14. Calculated grain boundary migration rate of different growth modes as a function of temperature.

interfaces (e.g., Fig. 5f); thus, the growth rate in the longitudinal direction can be estimated using the following equation [36]:

$$v_L = \frac{\bar{D}}{4h} \frac{(C_0 - C_{\alpha 2})}{(C_\gamma - C_{\alpha 2})}, \tag{1}$$

$$\bar{D} = \bar{D}_0 \exp(-Q/kT), \tag{2}$$

where v_L is the longitudinal growth rate of the γ lamellae; $\bar{D}$ is the interdiffusion coefficient of Ti and Al atoms in the α_2 phase; C_0 is the Al concentration of the alloy; $C_{\alpha 2}$ and C_γ are the Al concentrations in the α_2 and γ phases under the equilibrium, respectively; h is the ledge height, and the ledges were observed as one or two close-packed layers in present studies; $\bar{D}_0$ is the pre-exponential factor of the interdiffusion coefficient, and its value is 1.3×10^{-3} m^2 s^{-1}; Q is the activation energy, which is approximately 3.26 eV [37]; k is the Boltzmann constant; and T is the temperature.

Based on the above equations, the growth rate of the lamellar structure in RS Ti-47Al-2Cr-2Nb alloys is calculated, and the result is presented in Fig. 14. It shows that the growth rate is extremely low ($\sim 10^{-3}$ nm min^{-1}) when the temperature is 600°C, and it exhibits an exponential increase as the temperature increases. When the temperature is elevated to 700 and 900°C, the values is approximately 1.1 and 827 nm min^{-1}, respectively.
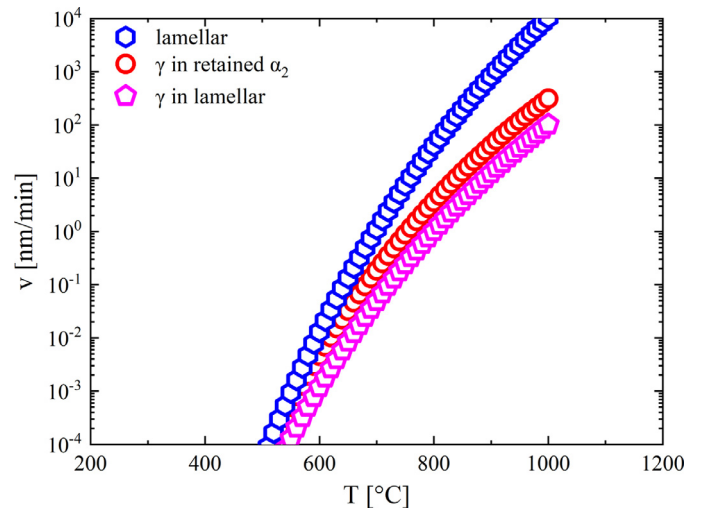
4.1.2. Equiaxed γ grains in the retained α_2 phase

Grain boundaries are the preferred heterogeneous nucleation sites for the γ grains because the interface energy of the nucleus is low at the grain boundaries, which has been demonstrated in previous studies [38]. Primary γ nuclei are also observed at the grain boundaries, in our experiments (Fig. 4(c3,d3)). Then, their growth process is determined by the grain boundary migration, which is a consequence of atomic motion [39]. The atomic motion is usually driven by the Gibbs free energies of adjacent grains, as schemati-
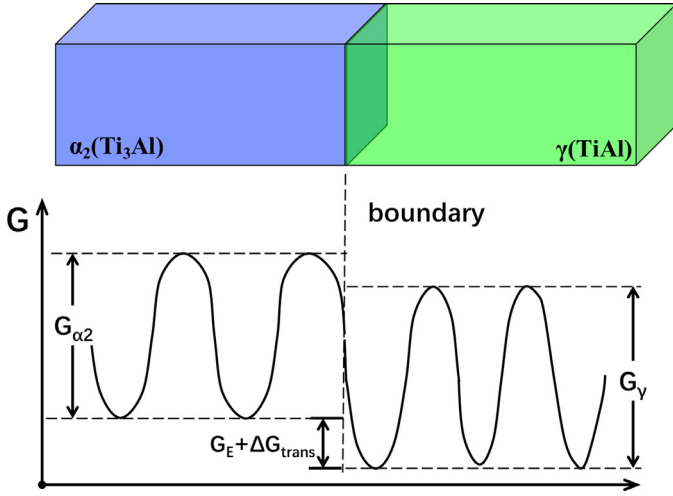
Fig. 15. Schematic of the atomic Gibbs free energy curve at a grain boundary when the equiaxed γ grains grow in the retained α_2 phase.

Table 1
Calculated cohesive energies (ϵ_0) and "raw" formation energies of point defects (ϵ_P) in α_2(Ti$_3$Al) and γ(TiAl) phases [36].

	ϵ_0(eV)	$\epsilon_{V_{Ti}}$(eV)	$\epsilon_{V_{Al}}$(eV)	$\epsilon_{Al_{Ti}}$(eV)	$\epsilon_{Ti_{Al}}$(eV)
Ti$_3$Al	-4.674	6.214	5.801	1.216	-0.591
TiAl	-4.396	6.257	5.092	1.859	-0.975

cally shown in Fig. 15. Thus, the grain boundary migration rate can be estimated as follows:

$$v = V^{1/3}\upsilon_0\left[A_2 \exp\left(-\frac{G_{\alpha 2}}{RT}\right) - A_1\exp\left(-\frac{G_{\alpha 2} + G_E + \Delta G_{trans}}{RT}\right)\right]. \tag{3}$$

Here, G_E represents the elastic strain energy stored in the retained α_2 phase, which is caused by the lattice distortion during the rapid solidification process; ΔG_{trans} is the difference in the Gibbs free energies between the α_2 and γ phases; V represents the atomic volume; υ_0 is the atomic vibration frequency; $G_{\alpha 2}$ is the activation energy to dislodge the atoms from the equilibrium locations in the α_2 phase, and A_2 is the probability of these atoms being received by the adjacent γ grain; and G_γ is the activation energy to dislodge the atoms from the equilibrium locations in the γ phase, and A_1 is the probability of these atoms being received by the adjacent α_2 grain.

Because grain boundary migration is a combined effect of both Ti and Al atoms in TiAl alloys, its growth rate can be estimated as follows:

$$v_\gamma = v_{Ti} + v_{Al}. \tag{4}$$

Here, v_γ represents the growth rate for the γ phase; and v_{Ti} and v_{Al} are the grain boundary migration rates caused by the Ti and Al atoms, respectively. Additionally, the parameters in the above equations can be estimated on the basis of experimental data and previous studies [37,40,41]. Firstly, G_E can be estimated an elasticity mechanics approach:

$$v_e = \frac{1}{2}\sigma_i\varepsilon_i, \tag{5}$$

$$\sigma_i = c_{ij}\varepsilon_j, \tag{6}$$

v_e is the elastic energy density and σ_i, ε_i and c_{ij} are the stress tensor, strain and elastic tensors; the elastic moduli of the α_2 and γ phases can be obtained from the previous studies [40,41]. For the RS powders, the lattice parameters of the retained α_2 phase were calculated on the basis of the XRD data; a and c are 5.8225 Å and 4.5912 Å, respectively. The ideal lattice parameters under the relaxation state are calculated; a and c are 5.7640 Å and 4.6640 Å, respectively. Thus, the elastic energy stored in the retained α_2 phase is estimated as $G_E = 3.23 \times 10^7$ J m^{-3}. Moreover, ΔG_{trans} is calculated as 3.13×10^8 J m^{-3} by Thermocalc software; $G_{\alpha 2}^{Ti}$ and

$G_{\alpha 2}^{Al}$ are respectively 2.0 and 2.1 eV; G_γ^{Ti} and G_γ^{Al} are respectively 2.2 and 2.5 eV [37]; and υ_0 is approximately 10^{13} s^{-1}[39].

The probability that the dislodged atoms are received by the adjacent grain is determined by the vacancy concentration at the boundary interface; thus, the interfacial concentration A can be estimated as $A = X_V^{2/3}$, where X_V is the volume concentration of vacancies. According to reference [37], the vacancy concentration X_V in a binary A_nB_m compound can be calculated using the following equations:

$$kT \ln \frac{X_{V_\alpha}}{X_{B_\alpha}^b} = b\epsilon_{B_\alpha} - \epsilon_{V_\alpha} - \epsilon_0, \tag{7}$$

$$kT \ln \frac{X_{V_\beta}}{X_{A_\beta}^a} = a\epsilon_{A_\beta} - \epsilon_{V_\beta} - \epsilon_0, \tag{8}$$

$$X_V = X_{V_\alpha} + X_{V_\beta}. \tag{9}$$

Here, a and b are the ideal stoichiometric factors, and $a = \frac{n}{n+m}$, $b = \frac{m}{n+m}$; the structure of the compound is assumed to consist of two sublattices, denoted as α and β, that are occupied by atoms A and B, respectively; V_α and V_β represent the vacancies on sublattices α and β, respectively; B_α and A_β represent the antisite defects on sublattices α and β, respectively; ϵ_0 represents the cohesive energy of an ideal compound; ϵ_{V_α}, ϵ_{V_β}, ϵ_{B_α}, and ϵ_{A_β} represent the "raw" formation energies of various point defects. The calculated cohesive energies (ϵ_0) and "raw" formation energies of point defects (ϵ_P) in α_2(Ti$_3$Al) and γ(TiAl) phases are shown in Table 1.

By synthesizing the Eqs. (3)–(9), the growth rate of equiaxed γ grains in retained α_2 phase can be calculated, as shown in Fig. 13e. Although the growth rate also shows an exponential increase trend as a function of temperature, the values are quite smaller than that of the lamellar structure. When the temperature is at 700 and 900°C, the associated growth rates are 0.18 and 41 nm min^{-1}, respectively.

4.1.3. Equiaxed γ grains in the nanolamellar structure

Guyon et al. [21,22] demonstrated that equiaxed γ grains can nucleate at the grain boundaries or inside the nanolamellar structures and subsequently grow up and consume the nanolamellar structures, thereby eventually transforming the lamellar structures into equiaxed γ microstructures during continuous heating. The high interfacial energy and the elastic strain energy stored in the nanolamellar structures, whose sum is $\sim$6.4 $\times$ 10^7 J m^{-3}, are considered to be the driving forces for this transformation. The atomic Gibbs free energy curve at the grain boundary where the equiaxed γ grains grow on the nanolamellar structure is illustrated in Fig. 16, and the associated boundary migration rate is calculated as:

$$v = V^{1/3}\upsilon_0\left[A_2 \exp\left(-\frac{G_\gamma}{RT}\right) - A_2\exp\left(-\frac{G_\gamma + G_E + G_b}{RT}\right)\right]. \tag{10}$$

Here, G_E and G_b are the interfacial energy and the elastic strain energy stored in the nanolamellar structure, and $G_E + G_b$ is approximately 6.4 $\times$ 10^7 J m^{-3} [22]. Combining Eq. (10) with Eqs. (4–9) yields the boundary migration rate in the nanolamellar structures.

Therefore, the growth rate of equiaxed γ grains in lamellar structure is obtained, which is shown in Fig. 14. Compared with
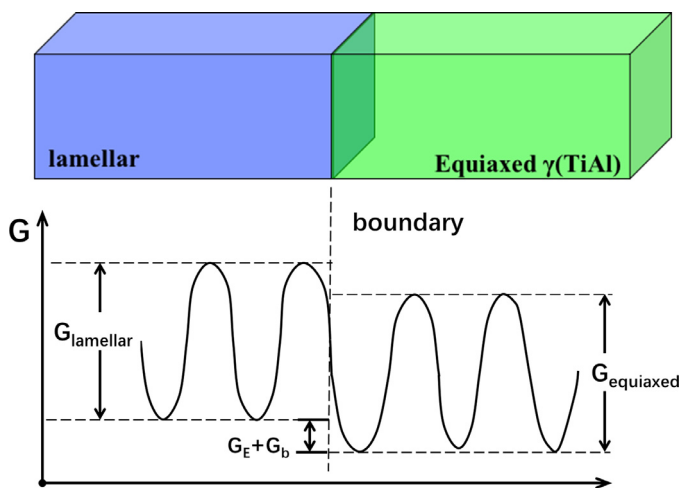
Fig. 16. Schematic of the atomic Gibbs free energy curve at a grain boundary when the equiaxed γ grains grow in the nanolamellar structure.

the above two conditions, its growth rate decreases further; the values are approximately 0.049 nm min^{-1} at 700°C and 12 nm min^{-1} at 900°C, respectively.

4.1.4. Competition of lamellar structures and equiaxed grains

Based on the calculated results above (Fig. 14), it is concluded that the lamellar structure grows the fastest; the equiaxed γ grains grow slower in the retained α_2 phase but exhibit the slowest growth in the nanolamellar structure. As the temperature increases, although all the growth rates increase greatly, they are clearly distinct, and the different microstructure selection is considered to result from the different growth rates. Combining these results with the microstructural characterizations, the microstructure evolution process can be inferred as follows:

(a) When the powders are aging-treated at 700°C, lamellae grow much faster than equiaxed γ grains; thus, they gradually fill the primary α_2 grains and manifest as the main feature during the aging treatment. When the lamellar structures filled the α_2 grains and connected with the equiaxed γ grains, growth mode of the equiaxed γ grains changes, and they grow by consuming nanolamellar structures, which contributes to a significant decrease in the growth driving force. Under such a condition, their growth rate drops to 0.049 nm min^{-1}, which is too small to cause any growth; thus, the lamellar structures remain as the aging time increases (Fig. 17a).

(b) When the powders are aging-treated at 900°C, the growth rates are high and sufficient for the growth of equiaxed γ grains in the nanolamellar structures. Although the lamellar structures quickly fill the primary α_2 grains, the equiaxed γ grains outgrow and destroy the preformed lamellar structures. Eventually, the powders completely transform into equiaxed γ microstructures (Fig. 17b).

4.2. Atypical pathway for $\alpha_2 \rightarrow \gamma$ lamellar transformation

Lamellar transformations in TiAl alloys have been studied extensively. It is commonly accepted that there are two ways to obtain the lamellar structure: (a) slow cooling from the high-temperature α phase region ($\alpha \rightarrow$ lamellar $\alpha/\gamma \rightarrow$ lamellar α_2/γ) and (b) performing aging treatment on the retained α_2 phase ($\alpha_2 \rightarrow$ lamellar α_2/γ) [32,42]. In either case, the γ phase essentially precipitates in the hcp structure, and the associated transformation mechanisms have been discussed in many reports. Denquin et al. [32] comprehensively analyzed many possible forma-

tion mechanisms and eventually proposed the most convincing mechanism based on the domain boundaries in γ laths. According to their study, the stacking faults move quickly in the longitudinal direction, which contributes to the formation of a metastable fcc phase in the matrix. Then, the chemical composition changes, and the metastable fcc phase transforms into an ordered γ phase. Pond et al. [43] further elaborated the mechanism as a displacive-diffusion transformation determined by diffusion-controlled ledge migration; the local fcc phase is the intermediate structure herein as well. However, the intermediate fcc phase was not observed. Although Cao et al. [44] discovered a metastable fcc phase during the inverse $\gamma \rightarrow \alpha_2$ transformation, the findings did not sufficiently prove that the fcc phase is an intermediate structure in the $\alpha_2 \rightarrow \gamma$ lamellar transformation.

In present studies, the RS microstructures retained the α_2 phase, and they could completely transform into lamellar structures at an aging temperature of 700°C. We recorded the primary stage of the lamellar structure transformation (Fig. 4-6). When the powders were aging-treated at 700°C for 5 min, there was an LPSO phase with the 6H structure in the retained α_2 phase, and very few γ lamellae were observed. However, when the aging time was increased to 30 min, the 6H structures completely disappeared, and the microstructure was predominantly composed of $\gamma/\gamma_{\text{twin}}$ lamellae. This phenomenon demonstrates that the 6H structure acts as an intermediate structure in the lamellar transformation. This is the first report in which the 6H intermediate structure was directly observed during the lamellar transformation process.

To analyze the transformation mechanism, the formation energies of various structures were calculated. Crystallographic data were established on the basis of the above characterizations (Table 2). In the table, the Ti–Al stochiometric ratio for α_2 and 6H is 3:1. The DFT calculations predict that the formation energy (FE) of 6H is approximately -265 meV/atom, and the negative value on the order of hundreds of meV/atom indicates that the 6H structure is significantly more stable than all other possible mixtures of the unary hcp Ti and fcc Al phases [13]. However, the α_2 phase has 15 meV/atom lower FE than the 6H structure, signifying that the α_2 phase is slightly more thermodynamically stable when the Al content is exactly 25 at.%. Because the FE is highly influenced by composition, Fig. 18a presents the FEs of the α_2 phase and 6H structure as a function of Al content. The FE of the α_2 phase first decreases when the Al content increases from 25 to 38 at.%, and then rapidly increases as the Al content increases to 50 at.%. However, the FE of the 6H structure shows a monotonically decreasing trend when the Al content increases from 25 at.% to 50 at.%. The FEs of these two structures are very close when the Al content ranges from 30 at.% to 38 at.%, and the FE of the 6H structure is further low when the Al content is approximately 35 at.%. Additionally, the XRD results reveal a large lattice elastic strain in the retained α_2 phase, and the elastic strains of a-and c-axes reach 1.02% and 3.26%, respectively. According to formulae (5) and (6), the average elastic energy in the retained α_2 phase is calculated as 3.23×10^7 J m^{-3} (equal to 6.825 meV/atom). The stored elastic energy increases the FE of the retained α_2 phase leading to a large high-formation-energy region (30–38 at.%) (Fig. 18a). Accompanied by the chemical and energy fluctuations in the powders, the formation of the 6H structure becomes possible. However, because of the much lower FE of the γ phase, the 6H structure will eventually transform into the γ phase to attain a state close towards equilibrium.

The structural characterization and energy analysis provide an alternative approach for the $\alpha_2 \rightarrow \gamma$ lamellar transformation that has seldom been mentioned before. Fig. 19 presents a plausible atomic schematic of the $\alpha_2 \rightarrow \gamma$ transformation with an intermediate 6H structure. First, stacking faults appear on every three close-packed layers in the α_2 phase, which locally changes the atomic stacking sequence, and the 6H structure forms. It is worth men-
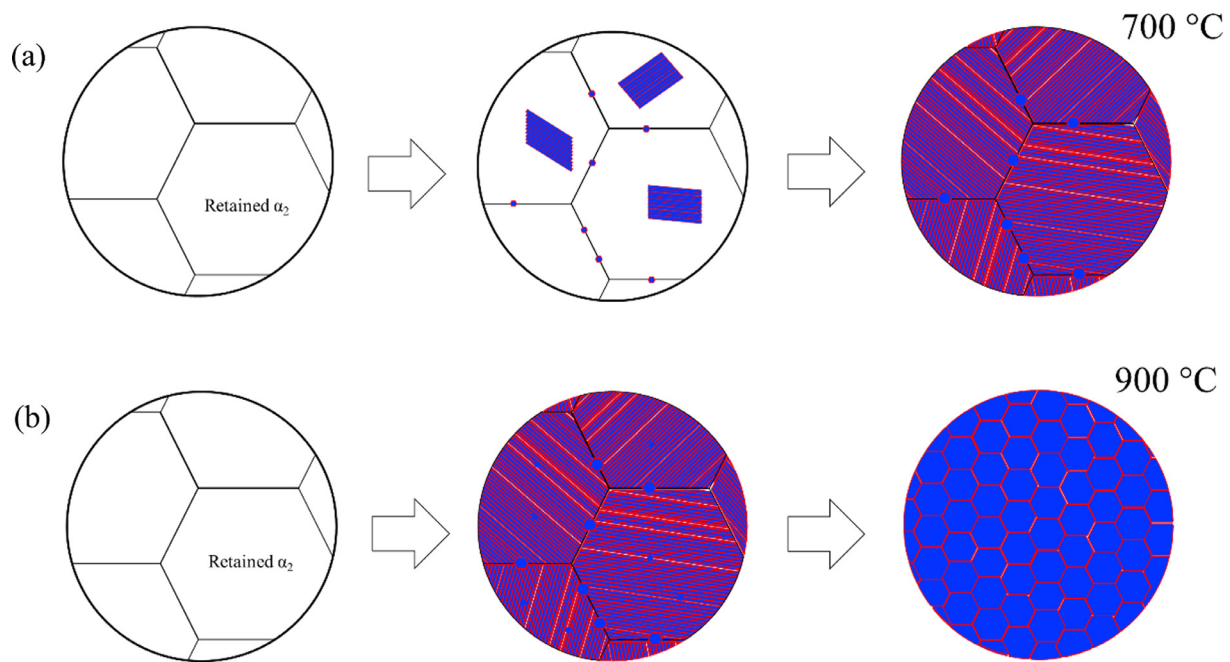
Fig. 17. Schematic of the microstructural evolution process for (a) lamellar microstructure and (b) equiaxed γ microstructure.

Table 2
Crystallographic data and formation energy (FE) for Ti–Al compounds.

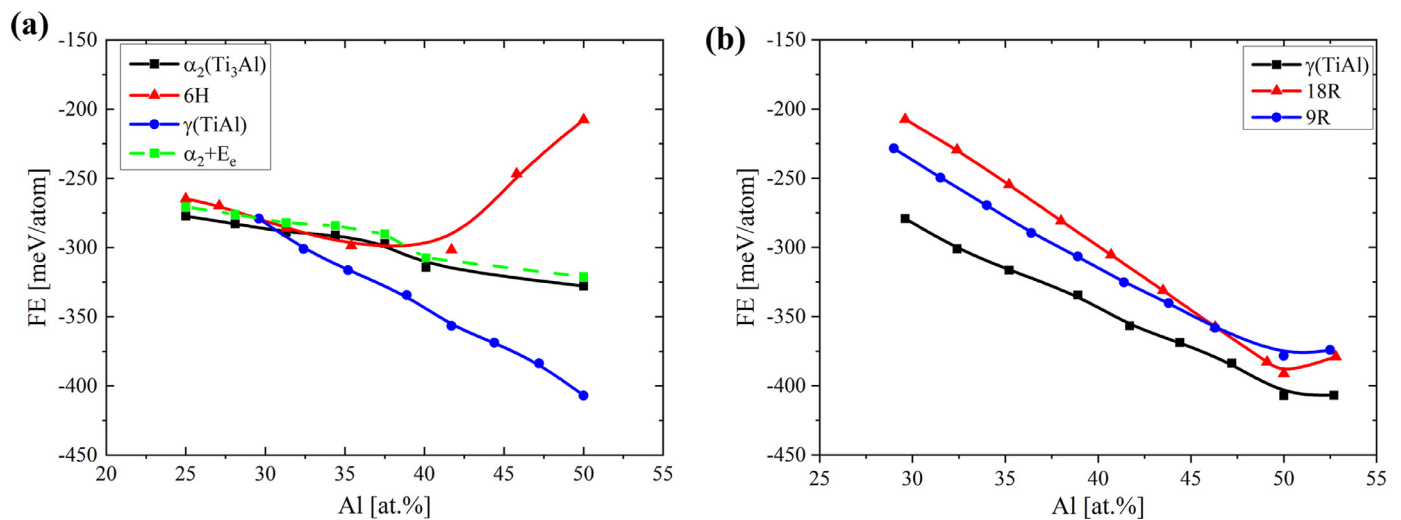| Compounds	Space Group	Lattice constant						FE (meV/atom)
		a (Å)	b (Å)	c (Å)	α	β	γ	
6H	P6$_3$/mmc (D6h)	5.714	5.714	13.994	90°	90°	120°	-265
α_2 (Ti$_3$Al)	P6$_3$/mmc (D6h)	5.734	5.734	4.644	90°	90°	120°	-280
9R	P2/m(C2h)	7.101	2.834	4.941	90°	76.959°	90°	-380
18R	P2/m(C2h)	13.934	2.809	4.975°	90°	84.8°	90°	-390
γ (TiAl)	P4/mmm (D4h)	3.977	3.977	4.079°	90°	90°	90°	- 400

Fig. 18. Calculated formation energies based on DFT method. (a) Comparison of α_2, 6H, γ, and γ+E$_e$ as a function of Al content. (b) Comparison of γ, 18R and 9R as a function of Al content.

tioning that the stacking faults that occur in the α_2 phase are alternately arranged negative stacking faults (A→C, B→A, C→B) and positive stacking faults (A→B, B→C, C→A), and the opposite stacking faults can not only minimize the net shear strain in the matrix [45] but also transform the hcp structure into a 6H structure (…ACACAC…→…ABCBCB→…ABCBAC). Because there is only one close-packed plane (0001) in the hcp α_2 phase, the precipitated 6H laths are always parallel to the (0001)$_{\alpha2}$ plane. In addition,

the …ABCBACA… type 6H structure can be considered to comprise many pseudo four-layer fcc laths. The pseudo four-layer fcc lath indicates that each lath possesses an incomplete four-layer fcc structure because the neighboring four-layer fcc laths share a common twinning plane. Moreover, these neighboring pseudo four-layer fcc laths exhibit a twin relationship, as shown in Fig. 19. This assumption can properly explain the 6H→γ transformation. The common twinning plane then migrates during the aging process,
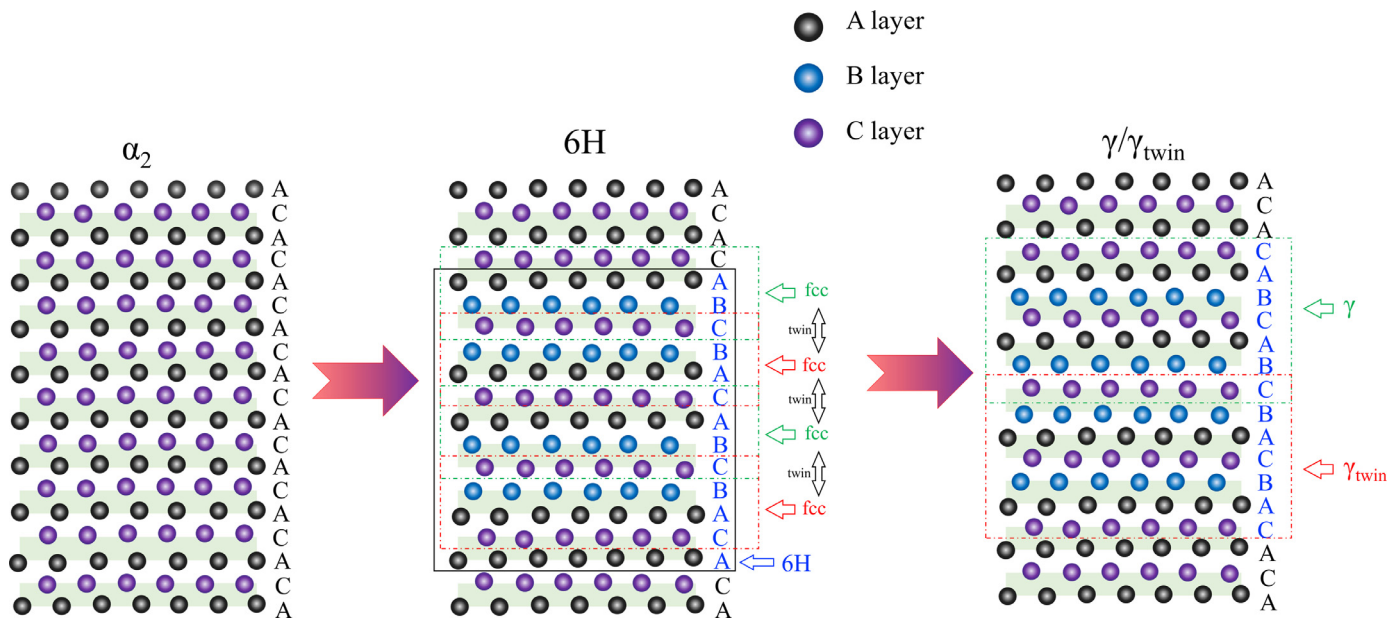
Fig. 19. Atomic schematic of the $\alpha_2 \rightarrow \gamma$ lamellar transformation with the 6H intermediate structure.

which coarsens these four-layer laths and transforms them into the real twinning laths. If this is the real transformation pathway, the wide 6H laths containing several pseudo four-layer fcc laths will decompose into many thin γ laths. Our experimental results corroborate this assumption; 10–30 nm width 6H laths first precipitate from the retained α_2 phase and then transform into nano γ laths, whose widths are measured to be only ~1 nm (Fig. 5d). Additionally, some studies have discovered that γ laths with opposite stacking sequences are evenly distributed in the lamellar structures when they transform from the retained α_2 phase [46]. This phenomenon can also be rationally explained by the experimental observation of equally distributed pseudo four-layer twin laths in the proposed transformation pathway. However, the extremely thin laths will coarsen to reduce the interfacial energy as the aging process continues; this is also demonstrated by our experiments (Fig5.d and f).

4.3. Formation of γ twins with the intermediate 9R and 18R structures

According to the observations and analyses of the powders aging-treated at 900°C, the retained α_2 phase first transforms into nanolamellar structures, and then evolves into equiaxed γ grains because of the high interfacial and elastic energies stored in nanolamellar structures. During this process, numerous dislocations and twins form in the equiaxed γ grains, accompanied by some LPSO phases. Additionally, these LPSO structures disappear and only γ twins are left in the equiaxed γ grains when the aging time is increased to 4 h, implying that these structures are metastable and will eventually transform into γ phase as the aging treatment continues. Here, we have discussed the formation of the 9R and 18R structures. First, their crystallographic data were established based on 1:1 Ti-Al stochiometric ratio (Table 2). The DFT results show that the formation energies of the 9R and 18R structures, although negative, are slightly higher than that of the γ phase (Fig. 18b). Thus, it is deduced that the 9R and 18R structures are energetically unfavorable. However, when the nanolamellar structure transforms into equiaxed γ grains, the high interfacial and elastic energies relax, thereby increasing the probability of the formation of crystal defects and metastable structures. This is demonstrated by the profuse dislocations observed in the equiaxed

γ grains (Fig. 9). Because the formation energies of 9R and 18R are only tens of meV/atom lower than that of the γ phase, these energetic barriers can be overcome and some LPSO phases can be locally formed during the transformation from lamellar structure to equiaxed grains. However, these structures are metastable and should transform into a more stable γ_{twin} during the subsequent aging treatment. This transformation behavior is demonstrated by our observations of the 9R/γ_{twin} transition region (Fig. 12). Thus, it is concluded that these LPSO phases can also play an intermediate role in the γ_{twin} transformation. Moreover, the stacking sequences of the 9R and 18R structures can be considered as the consequences of stacking faults on every three and six close-packed layer, respectively, in the γ phase; hence, stacking faults play an important roles in the transformation, and the detailed transformation mechanism should be investigated further.

5. Conclusion

In this study, the microstructure evolution mechanism of the rapidly solidified Ti–47Al–2Cr–2Na alloy was analyzed from the viewpoints of thermodynamics and kinetics, and the following conclusions were obtained:

(1) The rapidly solidified powders almost only retained the α_2 phase. The retained α_2 phase transformed into two different microstructures, namely, lamellar and equiaxed γ microstructures, depending on the temperature. The competition between the growth rates of lamellar and equiaxed γ microstructure determined the resultant microstructures.

(2) The LPSO phase with the 6H structure was observed at the early stage of aging process; it then transformed into narrow γ laths. This is the first study to directly demonstrate that the 6H structure can act as an intermediate phase in the $\alpha_2 \rightarrow \gamma$ transformation. The stacking sequence of the 6H structure was …ABCBACA…, and the driving force for the 6H structure is a result of the extremely high elastic energy stored in the retained α_2 phase.

(3) The LPSO phases with the 9R and 18R structures was observed in equiaxed γ grains when the powders were aging treated at 900°C; then, they disappeared and only γ/γ_{twin} remained. These structures originated during the growth process

of equiaxed γ grains, and the relaxation of the interfacial and elastic energies in nanolamellar structures triggered nucleation. Subsequently, the structures would transform into a more stable γ_{twin} phase.

Declaration of Competing Interest

There are no conflicts of interest.

Acknowledgement

References

[1] S.M. Thompson, L. Bian, N. Shamsaei, A. Yadollahi, An overview of direct laser deposition for additive manufacturing; part I: transport phenomena, modeling and diagnostics,, Addit. Manuf. 8 (2015) 36–62.

[2] N. Shamsaei, A. Yadollahi, L. Bian, S.M. Thompson, An overview of direct laser deposition for additive manufacturing; part II: Mechanical behavior, process parameter optimization and control, Addit. Manuf. 8 (2015) 12–35.

[3] Y.M. Wang, T. Voisin, J.T. McKeown, J. Ye, N.P. Calta, Z. Li, Z Zeng, Y. Zhang, W. Chen, T.T. Roehling, R.T. Ott, M.K. Santala, P.J. Depond, M.J. Matthews, A.V. Hamza, T. Zhu, Additively manufactured hierarchical stainless steels with high strength and ductility, Nat. Mater. 17 (2018) 63–70.

[4] H. Hou, E. Simsek, T. Ma, N.S. Johnson, S. Qian, C. Cisse, D. Stasak, N.A. Hasan, L. Zhou, Y. Hwang, R. Radermacher, V.I. Levitas, M.J. Kramer, M.A. Zaeem, A.P. Stebner, R.T. Ott, J. Cui, I. Takeuchi, Fatigue-resistant high-performance elastocaloric materials made by additive manufacturing, Science 29 (2019) 1116–1121.

[5] L.E. Murr, S.M. Gaytan, A. Ceylan, E. Martinez, J.L. Martinez, D.H. Hernandez, B.I. Machado, D.A. Ramirez, F. Medina, S. Collins, R.B. Wicker, Characterization of titanium aluminide alloy components fabricated by additive manufacturing using electron beam melting, Acta Mater 58 (2010) 1887–1894.

[6] W. Li, Y. Yang, J. Liu, Y. Zhou, M. Li, S. Wen, Q. Wei, C. Yan, Y. Shi, Enhanced nanohardness and new insights into texture evolution and phase transformation of TiAl/TiB$_2$ in-situ metal matrix composites prepared via selective laser melting, Acta Mater 136 (2017) 90–104.

[7] J. Wang, Q. Luo, H. Wang, Y. Wu, X. Cheng, H. Tang, Microstructure characteristics and failure mechanisms of Ti-48Al-2Nb-2Cr titanium aluminide intermetallic alloy fabricated by directed energy deposition technique, Addit. Manuf. 32 (2020) 101007.

[8] J. Schwerdtfeger, C. Korner, Selective electron beam melting of Ti-48Al-2Nb-2Cr: Microstructure and aluminium loss, Intermetallics 49 (2014) 29–35.

[9] M. Todai, T. Nakano, T. Liu, H.Y. Yasuda, K. Hagihara, K. Cho, M. Ueda, M. Takeyama, Effect of building direction on the microstructure and tensile properties of Ti-48Al-2Cr-2Nb alloy additively manufactured by electron beam melting, Addit. Manuf. 13 (2017) 61–70.

[10] X. Zhang, C. Li, M. Zheng, H. Zhong, J. Gu, Alternative-band microstructure and LPSO phase in TiAl alloy produced by direct laser deposition, Mater. Charact. 164 (2020) 110315.

[11] X. Zhang, C. Li, Q. Wang, M. Zheng, Z. Ye, J. Gu, Unusual ordered phases with long periodic stacking structures in an additively manufactured TiAl alloy, Mater. Res. Lett. 8 (12) (2020) 454–461.

[12] E. Abe, Y. Kawamura, K. Hayashi, A. Inoue, Long-period ordered structure in a high-strength nanocrystalline Mg-1 at% Zn-2 at% Y alloy studied by atomic-resolution Z-contrast STEM, Acta Mater 50 (15) (2002) 3845–3857.

[13] J.K. Kim, W.S. Ko, S. Sandlobes, M. Heidelmann, B. Grabowski, D. Raabe, The role of metastable LPSO building block clusters in phase transformations of an Mg-Y-Zn alloy, Acta Mater 112 (15) (2016) 171–183.

[14] M. Matsuda, S. Ii, Y. Kawamura, Y. Ikuhara, M. Nishida, Interaction between long period stacking order phase and deformation twin in rapidly solidified Mg$_{97}$Zn$_1$Y$_2$ alloy, Mater. Sci. Eng. A 386 (1-2) (2004) 447–452.

[15] M. Matsuda, S. Ando, M. Nishida, Dislocation structure in rapidly solidified Mg$_{97}$Zn$_1$Y$_2$ alloy with long period stacking order phase, Mater. Trans. 46 (2) (2005) 361–364.

[16] S.R. Singh, J.M. Howe, Studies on the deformation behaviour of interface in $(\gamma+\alpha_2)$ titanium aluminide by high-resolution transmission electron microscopy, Phil. Mag. Lett. 65 (2) (1992) 233–241.

[17] F. Appel, P.A. Beaven, R. Wagner, Deformation processes related to interfacial boundaries in two-phase γ-titanium aluminides, Acta Metall 41 (6) (1993) 1721–1732.

[18] J.G. Wang, L.C. Zhang, G.L. Chen, H.Q. Ye, Formation of stress-induced 9R structure in a hot-deformed Ti-45Al-10Nb alloy, Scripta Mater 37 (2) (1997) 135–140.

[19] L. Song, X.J. Xu, C. Peng, Y.L. Wang, Y.F. Liang, S.L. Shang, Z.K. Liu, J.P. Lin, Deformation behaviour and 6H-LPSO structure formation at nanoindentation in lamellar high Nb containing TiAl alloy, Phil. Mag. Lett. 95 (2) (2015) 85–91.

[20] C.L. Chen, W. Lu, Y.Y. Cui, L.L. He, H.Q. Ye, High-resolution image simulation of overlap structures in TiAl alloy, J. Alloys Compd. 468 (1–2) (2009) 179–186.

[21] J. Guyon, A. Hazotte, E. Bouzy, Evolution of metastable α phase during heating of Ti48Al2Cr2Nb intermetallic alloy, J. Alloy Compd. 656 (2016) 667–675.

[22] J. Guyon, A. Hazotte, F. Wagner, E. Bouzy, Recrystallization of coherent nanolamellar structures in Ti48Al2Cr2Nb intermetallic alloy, Acta Mater 103 (2016) 672–680.

[23] Z. Trzaska, A. Couret, J.P. Monchoux, Spark plasma sintering mechanisms at the necks between TiAl powder particles, Acta Mater 118 (2016) 100–108.

[24] G. Kresse, J. Furthmuller, Efficiency of ab-initio total energy calculations for metals and semiconductors using a plane-wave basis set, Comp. Mater. Sci. 6 (1) (1996) 15–50.

[25] J.P. Perdew, K. Burke, M. Ernzerhof, Generalized Gradient Approximation Made Simple, Phys. Rev. Lett. 77 (18) (1996) 3865–3868.

[26] H.J. Monkhorst, J.D. Pack, Special points for Brillouin-zone integrations, Phys. Rev. B 13 (12) (1976) 5188–5192.

[27] M. Charpentier, D. Daloz, E. Gautier, G. Lesoult, A. Hazotte, M. Grange, Study of Microstructure and Solute Partitioning in a Cast Ti-48Al-2Cr-2Nb Alloy by Quenching during Directional Solidification Technique, Metall. Mater. Trans. A 34 (2003) 2139–2148.

[28] D.Y. Yang, H.X. Peng, Y.Q. Fu, F.Y. Cao, Z.L. Ning, S. Guo, Y.D. Jia, N. Liu, J.F. Sun, Nucleation on Thermal History and Microstructural Evolution of Atomized Ti-48Al Nano and Micro-Powders, Nanosci. Nanotech. Let. 7 (7) (2015) 603–610.

[29] Y.M. Zhu, A.J. Morton, J.F. Nie, The 18R and 14H long-period stacking ordered structures in Mg-Y-Zn alloys, Acta Mater 58 (2010) 2936–2947.

[30] S.B. Mi, Q.Q. Jin, New polytypes of long-period stacking ordered structures in Mg-Co-Y alloys, Scripta Mater 68 (2013) 635–638.

[31] V.T. Witusiewicz, A.A. Bondar, U. Hecht, S. Rex, T.Ya. Velikanova, The Al–B–Nb–Ti system: III. Thermodynamic re-evaluation of the constituent binary system Al–Ti, J Alloys Compd 465 (1–2) (2008) 64–77.

[32] A. Denquin, S. Naka, Phase transformation mechanisms involved in two-phase TiAl-based alloys—I. Lamellar structure formation, Acta Mater 44 (1) (1996) 343–352.

[33] Z. Guo, A.P. Miodownik, N. Saunders, J.P. Schille, Influence of stacking-fault energy on high temperature creep of alpha titanium alloys, Scripta Mater 54 (12) (2006) 2175–2178.

[34] E.A. Metzbower, Stacking fault probability determinations in HCP Ti–Al alloys, Metall. Mater. Trans. B 2 (1971) 3099–3103.

[35] L.C. Zhang, T.T. Cheng, M. Aindow, Nucleation of the lamellar decomposition in a Ti-44Al-4Nb-4Zr alloy, Acta Mater 52 (2004) 191–197.

[36] G.H. Qin, S. Hao, X. Sun, Ledge mechanism of primary α_2/γ lamellae growing in the supersaturated α_2 matrix for γ-TiAl-based (γ/α_2) alloy, Scripta Mater 39 (3) (1998) 289–293.

[37] G. Lindwall, K.W. Moon, Z. Chen, M. Mengason, M.E. Williams, J.M. Gorham, J.C. Zhao, C.E. Campbell, Diffusion in the Ti-Al system, J. Phase Equilib. Diff. 39 (2018) 731–746.

[38] H. Zhu, D.Y. Seo, K. Maruyama, P. Au, Effect of microstructural stability on creep behavior of 47XD TiAl alloys with fine-grained fully lamellar structure, Scripta Mater 52 (1) (2005) 45–50.

[39] G. Gottstein, Physical Foundations of Materials Science, Springer, Berlin, 2004.

[40] C.L. Fu, J. Zou, M.H. Yoo, Elastic constants and planar fault energies of Ti3Al, and interfacial energies at the Ti$_3$Al/TiAl interface by first-principles calculations, Scripta Metall. Mater. 33 (6) (1995) 885–891.

[41] K. Xiong, X. Liu, J. Gu, Orientation-dependent crystal instability of gamma–TiAl in nanoindentation investigated by a multiscale interatomic potential finite-element model, Model. Simul. Mater. Sc. 22 (8) (2014) 085013.

[42] T. Klein, L. Usategui, B. Rashkova, M.L. No, J.S. Juan, H. Clemens, S. Mayer, Mechanical behavior and related microstructural aspects of a nano-lamellar TiAl alloy at elevated temperatures, Acta Mater 128 (15) (2017) 440–450.

[43] R.C. Pond, P. Shang, T.T. Cheng, M. Aindow, Interfacial dislocation mechanism for diffusional phase transformations exhibiting martensitic crystallography: formation of TiAl + Ti$_3$Al lamellae, Acta Mater 48 (5) (2000) 1047–1053.

[44] S. Cao, S. Xiao, Y. Chen, L. Xu, X. Wang, J. Han, Y. Jia, Phase transformations of the L1$_2$-Ti$_3$Al phase in γ-TiAl alloy, Mater. Des. 121 (5) (2017) 61–68.

[45] Y.M. Zhu, M. Weyland, A.J. Morton, K. Oh-ishi, K. Hono, J.F. Nie, The building block of long-period structures in Mg–RE–Zn alloys, Scripta Mater 60 (11) (2009) 980–983.

[46] S. Zghal, M. Thomas, S. Naka, A. Finel, A. Couret, Phase transformations in TiAl based alloys, Acta Mater 53 (9) (2005) 2653–2664.